

Surface tension driven flow of blood in a rectangular microfluidic channel: effect of erythrocyte aggregation.

D. Palias¹, A. Passos², G. Constantinides¹, S. Balabani² and E. Kaliviotis^{*1}

¹Dept. of Mechanical Engineering and Materials Science and Engineering, Cyprus University of Technology, 45 Kitiou Kyprianou, 3041, Limassol, Cyprus

²Dept. of Mechanical Engineering, University College London, Roberts Building, Torrington Place, WC1E 7JE, London, UK

*Corresponding Author. Email: e.kaliviotis@cut.ac.cy

Abstract: Microfluidic platforms have increasingly been explored for *in vitro* blood diagnostics and for studying complex microvascular processes. The perfusion of blood in such devices is typically achieved through pressure driven set-ups. Surface tension driven blood flow provides an alternative flow delivery option, and various studies in the literature have examined the behaviour of blood flow in such fluidic devices. In such flows, the influence of red blood cell (RBC) aggregation, the phenomenon majorly responsible for the non-Newtonian nature of blood, requires particular attention. In the present work, we examine differences in the surface tension driven flow of aggregating, non-aggregating RBC, and Newtonian suspensions, in a rectangular micro channel. The velocity fields were obtained using micro-PIV techniques. The analytical solution for blood velocity in the channel is developed utilising the power law model for blood viscosity. The results showed that RBC aggregation has an impact at the late stages of the flow, observed mainly in the bluntness of the velocity profiles. At the initial stages of the flow the shearing conditions are found moderately elevated, preventing intense RBC aggregate formation. As the flow decelerates in the channel RBC aggregation increases, affecting the flow characteristics.

Keywords: Surface tension driven blood flow, rectangular microchannel.

This is the author's peer reviewed, accepted manuscript. However, the online version of record will be different from this version once it has been copyedited and typeset.
PLEASE CITE THIS ARTICLE AS DOI:10.1063/1.50008939

Nomenclature:

Abbrev. / Symb.	Explanation	Units	Abbrev. / Symb.	Explanation	Units
AR	Aspect ratio (W/h)	-	h_p	Gap between the plates	μm
CV	Coefficient of variation	-	\bar{I}	Mean intensity	-
NA	Numerical aperture	-	k	Power law consistency index	Pa s^n
NAB	Non aggregative blood	-	L_e	Entrance length	μm
NF	Newtonian fluid	-	L_w	Wavelength of illumination	μm
PBS	Phosphate buffered saline	-	$L(t)$	Time-dependent meniscus position	μm
PIV	Particle image velocimetry	-	M	Image magnification	-
O_2	Oxygen	-	n	Power law index	-
ROI	Region of interest	-	N	Refractive index of air	-
SD	Standard deviation	-	P	Pressure	Pa
SD_I	Intensity standard deviation	-	Q	Flow rate per unit length	$\mu\text{m}^2 \text{s}^{-1}$
STD	Surface tension driven (flow)	-	r	Radius	μm
St	Stokes number	-	R_1, R_2	Radii of meniscus curvature	μm
TiO_2	Titanium dioxide	-	t	Time	s
UV	Ultraviolet	-	t_p	Particle response time	s
WB	Whole blood	-	t_f	Flow characteristic time	s
$ \dot{\gamma} $	Shear rate magnitude	s^{-1}	v	Linear velocity (plate flow)	$\mu\text{m s}^{-1}$
$\dot{\gamma}_{i-p}$	In plane shear rate component	s^{-1}	V_c^*	Normalized blood velocity in the Couette flow	-
ΔP_{Y-L}	Young-Laplace pressure difference	Pa	V_{ch}	Velocity in the core of the channel	$\mu\text{m s}^{-1}$
ε	Relative threshold value	-	\bar{V}_{ch}	Mean of V_{ch}	$\mu\text{m s}^{-1}$
θ_d	Dynamic contact angle	Deg.	V_{ch}^*	V_{ch} normalized with V_{max}	-
θ_c	Static contact angle	Deg.	V_m	Mean meniscus velocity	$\mu\text{m s}^{-1}$
μ	Dynamic viscosity	mPa	\bar{V}_m	Mean value of V_m	$\mu\text{m s}^{-1}$
μ_{NF}	Newtonian fluid dynamic viscosity	mPa	V_{max}	Maximum of V_{ch}	$\mu\text{m s}^{-1}$
μ_{P-L}	Power law viscosity	mPa	V_{m-an}	Theoretical meniscus velocity	$\mu\text{m s}^{-1}$
ρ	Density	Kg m^{-3}	V_{mean}	Theoretical mean core-flow velocity	$\mu\text{m s}^{-1}$
σ	Surface tension	Nm^{-1}	\bar{V}_{m-mean}	Mean of \bar{V}_m	$\mu\text{m s}^{-1}$
ω	Angular velocity	rad s^{-1}	V_p^*	Normalized plate velocity	-
Ca	Capillary number	-	V_{z-c}	Velocity in the flow core, z-dir.	$\mu\text{m s}^{-1}$
CO_2	Carbon dioxide	-	$V_{z-\sigma}$	Theoretical velocity profile, z-dir.	$\mu\text{m s}^{-1}$
D	Depth of correlation	μm	W	Width of the channel	μm
d_p	Particle diameter	μm	x^*	Normalized x-dir. ($x^*=x/W$)	-
d_h	Hydraulic diameter	μm	y^*	Normalized y-dir. ($y^*=y/W$)	-
h	Half height of channel	μm	z^*	Normalized x-dir. ($z^*=z/W$)	-

1 Introduction

Microfluidic technology has received considerable interest over the last decades.¹ Microfluidic devices allow for small sample manipulation and enable miniaturisation of laboratory techniques. Such devices have become increasingly popular in diagnostics and health care applications due to a number of advantages²: They are cost effective, can be used on site and are disposable making them very practical for research and clinical use.³ Furthermore, they offer tremendous potential in areas such as drug discovery, biosensing and chemical synthesis, where handling small volumes is critical.⁴

Microfluidic studies designed to mimic the microcirculation and probe the flows therein, utilise by default pressure-driven experimental set-ups. Pioneering studies using fluorescent and brightfield particle image velocimetry techniques allowed the detailed analysis of the flow in such applications.^{5,6} Lima *et al.*^{7,8} examined the effect of haematocrit (Hct) on microscale blood flow by utilising confocal micro-PIV techniques, using non-aggregating samples in a square microchannel. The velocity profiles were found parabolic, with considerable velocity fluctuations observed at increased haematocrits. The radial displacement of RBCs flowing through a 100 μm diameter tube was also examined; it was found that RBCs exhibit higher erratic radial displacement in dense (24-35% Hct) compared to dilute suspensions.⁸ The flow, and the structural and mechanical characteristics of blood in bifurcating microchannels (T-type) were examined in a series of studies by the authors,⁹⁻¹⁴ using aggregating and non-aggregating RBC suspensions; the flow split ratio between the parent and daughter branches was found to affect the haematocrit (and RBC flux), the aggregate size distribution (and aggregate flux), and the local viscosity of the fluid. Furthermore, RBC aggregation was found to increase the bluntness and skewness of the velocity profiles, and the properties of the cell depleted layer (CDL). Studies have shown that RBC clustering, which was not caused by RBC aggregation forces, takes place in confined flows,¹⁵ and that the therapeutic efficacy of microparticles used in drug delivery could be affected by the particle/RBC interaction in the vasculature.¹⁶ The effect of RBC aggregation on microscale blood flows has also been examined in a straight microchannel by Mehri *et al.*,^{17,18} illustrating the relationship between aggregate size, shear rate and viscosity and in an artificial microvascular network¹⁹ showing no effect of RBC aggregation on perfusion, but a haematocrit increase in the capillary scale branches of the network.

Pressure-driven flows require accurate pumping and tubing which may cause various difficulties for point of care diagnostics.²⁰ Surface tension driven (STD) blood flow offers a simpler and cost effective option to the pressure driven flows.^{4,21} Surface tension is a material property of a fluid-fluid interface whose origins lie in the different attractive intermolecular forces that act in the two fluid phases. STD flows depend on the hydrophilicity/hydrophobicity of the surface material. Hydrophilic materials have good affinity with fluids causing them to spread, whereas hydrophobic materials cause repulsion to fluids resulting in droplet formation.²² Various methods have been employed to improve the surface properties of the channel materials. The hydrophilicity of the surfaces can be improved with low power laser CO₂ ablation²³, oxygen plasma exposure^{24,25} and UV surface activation.²⁶ Surface wetting properties induced by plasma can be maintained for a few weeks.²⁷ Combining TiO₂ films with O₂ plasma etching treatment, and/or UV activation²⁸ has been found to further enhance wetting properties of glass surfaces.

In addition to surface treatment strategies, geometrical characteristics such as aspect ratio (AR) and turning angle are important in designing microchannels for STD flows. These characteristics have been examined in various studies and has been shown, that as the aspect ratio increases the velocity of the advancing liquid front increases for AR up to 1.5.²⁹⁻³² Chen *et al.*²⁹ also examined the flow characteristics in open micro channels with different turning angles (45° to 135° with respect to the horizontal plane) for Newtonian fluids; they reported that the meniscus decelerated at the turning region, and accelerated immediately after (for the 90° to 135° angles) reaching higher velocities than the incoming flow, before recovering back to its original incoming velocity.

Berthier *et al.*²⁰ studied the spontaneous capillary blood flow in a narrow V-groove microchannel and the maximum measured velocities were found to be up to 7.5 cm/s, decreasing non-linearly with time and distance, but remaining at relatively high magnitudes for a significant proportion of the channel length. Experimental observations agreed with the theoretical analysis of spontaneous capillary flows in open V-groove channels, based on a force balance between the capillary forces driving the flow, and the viscous friction at the walls resisting the flow. Kung *et al.*³⁰ studied STD blood flow in an inclined microchannel at different sloping angles (from -90° to +90°). Surprisingly, it was found that the blood flow rate was increased for upward motion (angle > 0°) while decreasing for downward flow (angles < 0°). This was

explained by the change in frictional force at different sloping angles, due to the haematocrit decrease in the upward flow case. Cito *et al.*²¹ examined the flow behind the advancing meniscus for water and blood, using rectangular and circular microchannels of various cross sections, and utilizing a spectral-domain Doppler optical coherence tomography technique for the visualisation of the flow; they showed that recirculation regions exist behind the meniscus, with developing velocities normal to the flow, which were comparable and even higher to the meniscus velocities. The results were then compared with the analytical predictions of the Lucas–Washburn equation assuming that blood behaves as a power-law non-Newtonian fluid and found to be in a reasonable agreement.²¹ Other theoretical studies have reported an initial acceleration followed by a flow deceleration as the capillary force is balanced by the inertia forces of the fluid.^{32,33} In a computational study analysing the exit effects on STD blood flow³⁴, it was shown that if the capillary tube has an open window at the end, the results agree with those of a simplified analytical solution³² within 5%. However, in the case that the capillary tube has a side exit opening instead of an opening facing the meniscus front, the effect of the air motion in front of the blood-air interface becomes more significant.

STD flows for diagnostic purposes have also been reported in the literature. Sneha Maria *et al.*²⁷ devised a rectangular polydimethylsiloxane (PDMS) microchannel, with differential wetting properties, in order to separate the plasma and detect the glucose levels therein. In another study³⁵ an on-chip whole blood/plasma separator was developed using a combination of asymmetric nanoporous super-hydrophilic surfaces and patterned hydrophobic patches. An asymmetric capillary force through the micro channel was attained to achieve the separation of plasma from whole blood. Red blood cells were continuously accumulated within the hydrophobic patch which worked as a naturally organized microfilter.³⁵

Despite the potential and increasing interest of STD flows in blood flow diagnostics, there are aspects in such flows which have not been systematically investigated to date; key properties of blood such as RBC aggregation have not been considered thoroughly. RBC aggregation is a major determinant of blood viscosity³⁶ and it has been shown to affect local microscale flow characteristics.⁹ In the present study, we examine the influence of the RBC aggregation phenomenon on surface tension driven flows in rectangular micro channels. Aggregating and non-aggregating blood samples were tested; their flow characteristics

were determined using micro-PIV based techniques and compared to those for a Newtonian fluid flowing in the same channel.

2 Methodology

2.1 Sample Preparation

The study was approved by the Cyprus Bioethics Committee (ref: EEBK/EP/2016/18). 5 blood samples were acquired from healthy volunteers into 4ml vacuum tubes (BD) preloaded with 1.8 mg/ml EDTA. Whole blood (WB) was used for aggregating blood experiments whereas non-aggregative blood samples (NAB) were produced by washing RBCs twice in Phosphate Buffered Saline (PBS), centrifuging at 3600 rpm for 10 minutes, and re-suspending them in PBS. WB and NAB samples were both adjusted at a haematocrit of 45% by adding/subtracting plasma. For consistency all experiments were conducted with a single sample. The consistency was further examined by duplicating/triplicating tests where appropriate. Newtonian flows were also examined using milk/water solutions (1:3 concentration respectively). Milk particles were used as tracers for the μ PIV-based analysis of Newtonian fluids (NF), as in previous studies.³⁷

2.2 Microfluidic channel fabrication.

The micro channel was made of glass slides (Superfrost, 1mm thickness) and double sided tape (3M, 100 μ m thickness, resulting in 100 μ m microchannel height) as shown in Figure 1, an approach similar to that used in Junker *et al.*³⁸ The aspect ratio ($AR=W/h$) was approximately 3, and the channel length 10 mm. Part of the bottom glass slide was left protruded to accommodate the blood drop. In the present work the variables x , y and z , are normalized with the width of the channel ($W\sim 300\ \mu\text{m}$) and expressed as x^* , y^* and z^* . The origin of the coordinate system was taken at the midplane of the channel, at the entrance. All measurements were performed in the region from $z=600\ \mu\text{m}$ from the entrance of the channel to a distance of $\sim z=1700\ \mu\text{m}$ to avoid any entrance effects, as in²¹: An entrance length (L_e) of 3.5 times the channel height (350 μm in the present case) for capillary flow in a rectangular channel, is sufficient to ensure fully developed flow.³⁹

Figure 1

2.3 *Experimental setup and procedures.*

Figure 2 shows a schematic of the experimental setup using the brightfield μ PIV system. The micro channel was placed horizontally on an upright microscope stage (OLYMPUS BX51). A 50 μ l drop of fluid was placed on the protruding part, of the bottom glass slide and at the entrance to the channel using a micropipette. The fluid was then set in motion through the channel due to the action of surface tension. The flow was recorded with a CMOS camera (IDT X3, at 625 fps) attached on the microscope (10X-objective NA=0.25) and analysed using JPIV (www.jpiv.vennemann-online.de) and Matlab software. The spatial resolution of the optics was 1.65 μ m/pixel.

Figure 2

2.4 *Contact angles and surface tension*

Static contact angle measurements were performed by capturing drop images (Figure 3) at the surfaces of contact (glass and adhesive tape), and then analysing the images using ImageJ software. The contact angle measurement set-up consisted of a usb camera, aligned with the XZ surface plane (Figure 1) of the specimen. Both camera and specimen were secured on a horizontally levelled stand. A drop of 10 μ l volume was applied with a micropipette on the surface of the specimen. The drop surface and drop contact lines were identified through image processing using the software ImageJ. The contact angle θ_c was defined as the angle between the line of contact and the surface line of the drop, measured counterclockwise (Figure 3c and 3d). When the wettability is high, small contact angles ($\ll 90^\circ$) and large base diameters occur (Figures 3a-c), whereas when wettability is low large contact angles ($\gg 90^\circ$) and smaller base diameters are apparent (Figure 3d).⁴⁰

Figure 3

The static contact angles of the fluids on the hydrophilic glass surfaces were found to be 36°, 38° and 44° for the NAB, WB and NF fluids respectively, forming a drop base diameter of approximately 5 mm (Figures 3a, b and c). Contact angles on the adhesive tape were found to be 100°, 96°, 110°, for the NAB, WB and NF fluids respectively, indicating the neutral/hydrophobic nature of the side, as opposed to the top and bottom walls of the channels (Figure 3d). The drop base diameters for the aforementioned cases were found to be approximately 3 mm.

Sample images of the surface tension driven microchannel flows of WB and NF are shown in Figure 3e. The angle that the marching meniscus forms with the side walls of the channel (the adhesive tape) is the dynamic contact angle, denoted by θ_d , which is also an index of wettability.⁴⁰ In the present case θ_d was calculated from the meniscus profile at each time-step. A best line of fit was created at the meniscus profile close to the side-wall, and θ_d was evaluated using: $\theta_d = \tan^{-1} \frac{\Delta x}{\Delta z}$. The meniscus, is seen, to have a slight paraboloid, or even a uniform shape, due to the non-hydrophilic properties of the side walls (double sided adhesive tape). Figure 3f shows a representative dynamic contact angle θ_d against time, illustrating that the meniscus profile becomes nearly flat as the dynamic contact angle reaches $\sim 85^\circ$ very shortly. The hydrophobicity/neutrality of the side boundaries does not promote the meniscus flow, which is driven by the surface tension forces developed at the top and bottom boundaries; it should be noted that the top/bottom dynamic contact angles could not be measured in the current set-up.

Surface tension values were measured for each fluid using a Kruus 100 surface tensiometer and found to be 0.022 Nm^{-1} , 0.023 Nm^{-1} and 0.020 Nm^{-1} for the NF, NAB and WB respectively.

2.5 μ PIV processing

A representative image from the flow of blood in the microchannel configuration is shown in Figure 1. The images were processed using the open source software JPIV to resolve the velocity field, and Matlab software was used for the analysis of the data. Three passes with interrogation windows (IW) of height and width of 32, 16 and 8 pixels were used for the μ PIV processing on the acquired images. Invalid vectors were replaced by the median of the neighbouring vectors. In the present study, a $13.2 \mu\text{m}$ vector spacing (for 10 X magnification) was achieved. Velocity profiles were calculated by axially averaging all of the velocities in a region of interest (ROI) after the meniscus had progressed in the channel.

2.6 Validation of the μ PIV technique.

It is well established that brightfield micro-PIV techniques suffer from relatively large depth of correlation fields (D),⁴¹ which lead to an underestimation of the velocity magnitude. Poelma *et al.*⁴² have shown that for relatively low magnifications in the μ PIV set-up the measured velocity is 33% lower than the actual flow velocity. D can be estimated using the following equation⁴¹:

$$D=2 \left[\frac{(1-\sqrt{\epsilon})}{\sqrt{\epsilon}} \left\{ \frac{N^2 d_p^2}{4NA^2} \right\} + \left\{ \frac{5.95(M+1)^2 L^2 N^4}{16M^2 NA^4} \right\} \right]^{\frac{1}{2}} \quad (1)$$

where d_p is the particle diameter, L_w the wavelength of illumination, M the image magnification, N is the refractive index of air, and NA the numerical aperture of the lens. ϵ is the relative threshold over which particles no longer contribute to the evaluation of displacement-correlation peak, which normally takes the value of 0.01. Hence, it can be considered that the measured velocity information represents the mean velocity of RBCs in the depth D , as the latter was calculated to be $99 \mu\text{m}$.

In order to assess the brightfield μPIV technique employed in the present study three methods were utilised. In the first method the velocity of RBCs (45% concentration) in a plate-plate system (CSS450 LINKAM SCIENTIFIC - see Figure 4 for a diagrammatic representation) was measured experimentally and compared with the analytical solution for the particular flow. More specifically, a thin film ($\sim 150 \mu\text{m}$) of whole blood was applied at the bottom plate of the plate-plate system of Figure 4. The upper plate of the system was not placed, and the bottom plate was then rotated at different constant rotational speeds ($\omega = 0.13$ and 0.8 rad s^{-1}). The velocity field was determined from the acquired images using JPIV. The linear velocity of the plate in the area of observation is given by $v=\omega r$ for a range of radius r , from $r=7.1$ mm to $r=7.9$ mm and constant angular velocity ω .

Figure 4

In the second method, simple Couette flows were generated between the bottom and the upper plate of the system (with the gap between the plates set at $h_p=100 \mu\text{m}$). The blood sample was placed between the plates and the microscope was focused at a height of $50 \mu\text{m}$ from the bottom plate. The bottom plate was rotated at two angular speeds ($\omega = 0.13$ and 0.8 rad s^{-1}) producing shear rates of 10 and 60 s^{-1} respectively. μPIV measurements were performed as described previously using the JPIV software.

The expected velocity profile for a narrow gap of $h=50 \mu\text{m}$ was also calculated analytically for the lower plate rotating at an angular velocity ω and the upper plate held stationary:

$$v=r\omega\left(1-\frac{z}{h_p}\right) \quad (2)$$

with $z = 50 \mu\text{m}$, and r from 7.1 to 7.9 mm.

Figure 5

Figures 5a and 5b compare the measured velocity profiles against the theoretical one for the first validation method (thin film of blood rotating on plate), illustrating good qualitative agreement (velocity data have been normalized with their values at the centre of the flow). Absolute velocity values were lower than theoretical ones by $\sim 10\%$ and $\sim 30\%$ for the 0.13 and 0.8 rad s^{-1} angular velocities respectively. Figures 5c and 5d show the comparison between measured and analytical normalized velocities for the Couette flow developed in the gap of the shearing system. The angular velocities were kept the same as in the previous test case, 0.13 and 0.8 rad s^{-1} , resulting in shear rates of 10 s^{-1} and 60 s^{-1} ; the observed velocity underestimation was $\sim 20\%$ and $\sim 30\%$ respectively. The underestimation in the velocity magnitude calculated with the μPIV technique is $\sim 30\%$ maximum, in agreement with discrepancies reported in other studies.⁴² The large depth of field, D , also means that the flow regions closer to the objective will contribute more to the PIV analysis, than the regions further away. The velocities in these regions are smaller (since they are closer to the top, fixed plate) which might further bias the measured (underestimated) velocities.⁴²

In a third validation exercise, the velocity field of the Newtonian STD flow in a microchannel ($AR \sim 3.7$) was measured, utilising a laser based micro-PIV technique using fluorescent particles as tracers (Nile Red, $\sim 1 \mu\text{m}$ size, at 1% concentration) suspended in distilled water, and compared against brightfield μPIV measurements (JPIV software) using milk particles as tracers in a $1:3$ milk/water Newtonian solution. The experimental setup for the fluorescent μPIV experiments is described in previous studies by Zhang *et al.*^{43,44} The system comprised a 16 Hz Nd-YAG laser source at 532 nm (Litron Laser, UK) for illumination, and a sCMOS camera (Xyla 5.5, Andor, UK) integrated on a bespoke microscope assembly ($10\times$ objective, $NA = 0.28$), for image acquisition. The spatial resolution of the technique was $0.56 \mu\text{m}/\text{pixel}$ and the depth of correlation was estimated to cover the entire flow depth.

Figure 6a shows an annotated schematic of the laser based μPIV system, and Figure 6b compares the measured velocity profiles (both profiles are normalized by the maximum measured velocity). Qualitatively the two profiles show very good agreement. The slightly increased bluntness of the velocity profile measured with the laser micro-PIV technique, could be attributed to technique-specific issues (differences

in correlation depth, etc.). The decrease in the velocity gradient near the side-walls of the channel is mainly due to the non-uniformity of the side-walls of the channels (adhesive tape), in which existing micro-pockets created regions of persistently low velocity. Direct comparison of velocity magnitudes between the measurement techniques show a maximum difference of ~15% with the velocity in fluorescent μ PIV being higher.

Figure 6

The Stokes number of the tracer particles can be calculated from $St = \frac{t_p}{t_f}$, where t_p is the particle characteristic response time, given by $t_p = \frac{\rho_p d_p^2}{18 \mu_{NF}}$, with particle density $\rho_p = 1050 \text{ kg m}^{-3}$, particle nominal diameter $d_p = 1 \mu\text{m}$ and Newtonian fluid viscosity $\eta_{NF} \approx 1.5 \cdot 10^{-3} \text{ Pa s}$ (see next section on viscosity measurements).⁴⁵ t_f is a flow characteristic time defined as $t_f = \frac{d_h}{\bar{V}_{PIV}}$. \bar{V}_{PIV} is the mean velocity of the flow, here calculated by the PIV technique and found to be in the order of 3 mm s^{-1} , and d_h is a characteristic diameter (hydraulic) of the channel equal to 150 microns. St was found to be in the order of 10^{-8} , indicating a negligible particle response time to the dynamics of the flow.

2.7 Viscosity measurements

Viscosity measurements were performed using a Brookfield DVIIT instrument, utilising a cone-plate geometry. Samples were loaded in the plate of the viscometer with a micropipette (0.6 ml volume) and tests were initiated approximately 30 seconds afterwards. Viscosities were measured by ramping down shear rates from 400 to 12.5 s^{-1} ; in order to ensure initial RBC aggregate dispersion. The maximum shear stress that cells were exposed at the highest shear rate was approximately 2 Pa for 30 seconds. The duration of a complete viscosity test was 8 minutes (16 points of measurement for 30 seconds each), and the viscosity measurement was performed at the end of the shearing period at each point. All measurements were performed at room temperature ($25 \pm 0.5 \text{ }^\circ\text{C}$). A power law model was used to fit the data from the viscosity measurements ($\mu_{p_L} = k\dot{\gamma}^{n-1}$).⁴⁶

Figure 7

Viscosity curves of the three working fluids are shown in Figure 7 for shear rates ranging from 12.5 s^{-1} to

400 s⁻¹. As expected whole blood exhibits a shear thinning behaviour mainly due to RBC aggregation. The non-aggregating sample (RBCs in PBS medium) exhibits a smaller decrease in viscosity with increasing shear rate, which is mainly due to the deformation of RBCs. The viscosity of the Newtonian solution is effectively constant at ~1.68 mPa s. The power law viscosity model ($\mu_{P_L}=k\dot{\gamma}^{n-1}$) was used to fit the viscosity data for both the WB and NAB blood suspensions, similarly to other studies.⁴⁶ The consistency indices k and the exponent n for the WB and NAB cases are shown in Table 1 and are in agreement with reported values in the literature.⁴⁶

Table 1: Power law coefficients and R ² values of blood samples.			
Sample	k [mPa s ⁿ]	n [-]	R ²
WB	26.200	0.302	0.973
NAB	7.134	0.123	0.991

2.8 Analytical solutions

2.8.1 Mean meniscus velocity

The theoretical mean axial (z-direction) meniscus velocity in STD flows can be calculated analytically as in previous studies^{21,47}, using the incompressible Navier-Stokes (N-S) equations, under the assumptions that the flow is fully developed, and one-dimensional, influenced mainly by the smaller dimension of the geometry (i.e. the height, 2h, of the channel, in the y direction for the coordinate system chosen for this study). The latter is due to the smaller radius of the meniscus curvature in the y-direction, compared to the one in the width direction (x). Under these assumptions, the continuity and z-momentum equations in the N-S equations reduce to:

$$\frac{\partial v_{z-\sigma}}{\partial z} = 0 \quad (3)$$

and

$$-\frac{1}{\rho} \frac{\partial P}{\partial z} + \frac{\mu}{\rho} \frac{\partial^2 v_{z-\sigma}}{\partial y^2} = 0 \quad (4)$$

μ is the dynamic viscosity of the fluid, and $\partial P = P_1 - P_0$. However, since the channel is open ended P_1 is equal to atmospheric pressure resulting to $\partial P = -P_0$ leading to $\frac{\partial P}{\partial z} = \frac{-P_0}{L}$. L is the meniscus position from the entrance. ∂P can be approximated with the Young-Laplace pressure drop:

$$\Delta P = \sigma \left(\frac{1}{R_1} + \frac{1}{R_2} \right) \quad (5)$$

R_1 and R_2 are the radii of curvature on the top and side walls of the channel respectively. As mentioned above, due to the high aspect ratio of the channel, the radius of curvature along the width W is much higher, compared to that along the height $2h$, hence the term $1/R_2$ is small compared to $1/R_1$ and considered negligible. This assumption results to $\Delta P_{Y-L} = \frac{2\sigma \cos(\theta_c)}{2h}$ and therefore:

$$\frac{\partial P}{\partial z} = \frac{\sigma \cos(\theta_c)}{hL} \quad (6)$$

Inserting Eq.(6) into Eq. (4):

$$\frac{\sigma \cos(\theta_c)}{hL} + \mu \frac{\partial^2 V_{z-\sigma}}{\partial y^2} = 0, \quad (7)$$

Integrating Equation (7) once, and applying the condition $\frac{\partial V_{z-\sigma}}{\partial y} = 0$ at $y = 0$, for a velocity maximum at the centre of the channel yields: $\mu \frac{\partial V_{z-\sigma}}{\partial z} = -\frac{\sigma \cos(\theta_c)}{hL} y$. By using the power law shear stress $\mu \frac{\partial V_{z-\sigma}}{\partial y} = k \left[\frac{\partial V_{z-\sigma}}{\partial y} \right]^n$ the equation becomes $k \left[\frac{\partial V_{z-\sigma}}{\partial y} \right]^n = -\left(\frac{\sigma \cos(\theta_c)}{hkL} \right)^{1/n}$ and can be solved using the no-slip boundary condition at the wall $V_{z-\sigma} = 0$ at $y = h$:

$$V_{z-\sigma} = \left(\frac{n}{n+1} \right) \left[\frac{\sigma \cos(\theta_c)}{khL} \right]^{\frac{1}{n}} \left[h^{1+\frac{1}{n}} - y^{1+\frac{1}{n}} \right] \quad (8)$$

For $n=1$, the parabolic Newtonian profile is recovered. The flow rate can be calculated from the velocity profile $V_{z-\sigma}$:

$$Q = 2W \int_0^h V_{z-\sigma} dy = 2W \left(1 + \frac{1}{n} \right) \left[\frac{\sigma \cos(\theta_c)}{khL} \right]^{\frac{1}{n}} \left[h^{\frac{2n+1}{n}} \left(1 - \frac{n}{2n+1} \right) \right] \quad (9)$$

The mean velocity in the core of the flow can be calculated as $V_{\text{mean}} = Q / hW$:

$$V_{\text{mean}} = \left(1 + \frac{1}{n} \right) \left[\frac{\sigma \cos(\theta_c)}{hkL} \right]^{\frac{1}{n}} \left[h^{\frac{n+1}{n}} \left(1 - \frac{n}{2n+1} \right) \right] \quad (10)$$

Assuming that the mean velocity of the meniscus (V_m) is equal to the mean velocity in the core of the flow (i.e. $V_m = V_{\text{mean}}$), the meniscus position as a function of time ($L=L(t)$) can be estimated using:

$$\frac{dL(t)}{dt} = V_{\text{mean}} \quad (11)$$

Therefore,

$$L(t) = h \left[\frac{\sigma \cos(\theta_c)}{hk} \right]^{\frac{1}{n+1}} \left[1 - \frac{n}{2n+1} \right]^{\frac{n}{n+1}} t^{\frac{n}{n+1}} \quad (12)$$

The time dependent marching meniscus velocity can be estimated analytically from the position $L(t)$:

$$V_{m-an} = \frac{dL(t)}{dt} = h t^{\left(\frac{-1}{n+1}\right)} \left[\frac{\sigma \cos(\theta)}{kh} \right]^{\frac{1}{n+1}} \left[\frac{n}{n+1} \right] \left[1 - \frac{n}{2n+1} \right]^{\frac{n}{n+1}} \quad (13)$$

The solution for the mean meniscus velocity (V_{m-an}) is similar to other solutions in the literature²¹ for the flow in the circular capillary duct.

2.8.2 Two-dimensional velocity profile in the core of the flow

The mean meniscus velocity was derived in the previous section based on Eq. 8, assuming negligible influence from the side boundaries (i.e., $V_{z-\sigma} = V_{z-\sigma}(y)$). For the analysis of the velocity field in the core of the flow, however, a complete analytical solution in both x and y directions is required for comparison with the experimental data. The 2-dimensional analytical solution for the velocity of pressure-driven flows in straight rectangular microchannels exists for a Newtonian fluid.⁴⁷ The boundary conditions in such a case also require zero velocity at all boundaries, i.e. $V_z = 0$ at $x = \pm W/2$, and at $y = 0$ and $2h$ (bottom and top plate for this solution), which are satisfied using a Fourier series expanded along the short, vertical y direction.⁴⁷ For the central plane of the microchannel, and when the Young-Laplace pressure is used as the flow driving mechanism the solution for the central plane in the geometry takes the following form:

$$V_{z-c} = 8W^2 \frac{\sigma \cos \theta_c}{\pi^3 \mu 2hL} \sum_{n, \text{odd}}^{\infty} \frac{1}{n^3} \left[1 - \frac{\cosh\left(\frac{n\pi y}{2h}\right)}{\cosh\left(\frac{n\pi}{2}\right)} \right] \quad (14)$$

The value of L can be set from the experimental data or from Equation 12 above, and will affect the behaviour of V_{z-c} quantitatively. The analytical solution V_{z-c} will be used to assess the deviation of the experimental velocity profiles from the Newtonian behaviour. The viscosity values used were 1.68, 4.41 and 8 mPa s, i.e. the mean values for the NF, NAB and the WB samples respectively.

2.9 Pressure – viscosity ratio

The main factors influencing the velocity of the flow are the surface tension σ , the viscosity of the fluids μ , and the wettability of the top-bottom channel surfaces quantified by the contact angle θ_c . Surface tension σ and wettability (contact angle θ_c) can be used to calculate the Young-Laplace pressure

difference ΔP_{Y-L} using $\Delta P_{Y-L} = \frac{\sigma \cos(\theta_c)}{h}$. The ratio $\Delta P_{Y-L} / \mu$ could provide meaningful information about the interrelationships between the aforementioned factors. Table 2 shows that the pressure/viscosity ratio is found to be higher in the NF fluid ($188.4 \cdot 10^{-3} \text{ s}^{-1}$), compared to NAB and WB ($84.4 \cdot 10^{-3}$ and $39.4 \cdot 10^{-3} \text{ s}^{-1}$ respectively). Thus the flow of NF is expected to be favoured compared to the other fluids, with WB been affected mostly by the higher viscosity. Table 2 shows the measured and aforementioned quantities in comparison.

Sample	σ (Nm ⁻¹)	θ_c (°)	μ (mPa s)	ΔP_{Y-L} (Pa)	$\Delta P_{Y-L} / \mu$ (s ⁻¹)
WB	0.020	38	8	315.2	$39.4 \cdot 10^{-3}$
NAB	0.023	36	4.41	372.1	$84.4 \cdot 10^{-3}$
NF	0.022	44	1.68	316.5	$188.4 \cdot 10^{-3}$

3 Results and discussion

3.1 Meniscus velocity

The meniscus velocity (V_m) was calculated for the initial stages of the flow until approximately 0.07 seconds, and L between 0.68 and 1.7 mm. First the meniscus position in the z-direction was found at each time-step, using Matlab image processing algorithms (see Figure 8a for the results from 45 images of a representative WB sample). The meniscus velocity V_m was then calculated by computing the distance covered by the meniscus (ΔL) at each time-step (Δt): $V_m = \frac{\Delta L}{\Delta t}$, with $\Delta t = \frac{1}{625}$, based on the frame rate used in image capturing. The mean velocity, \bar{V}_m , of the advancing meniscus was calculated as the average in the x-direction, and is shown in Figure 8b (black rectangles) against the analytical solution V_{m-an} (solid blue line). The experimental parameters n , k , σ , h and θ_c (Tables 1 and 2) have been used in V_{m-an} for the WB sample in Figure 8b.

Figure 8

Figure 8b shows that the flow accelerates during the initial observation time ($\sim 0.07 \text{ s}$). This acceleration is mainly due to the capillary forces, which dominate over other competing, mainly viscous, forces at the initial stages of the flow. This initial flow acceleration has been confirmed by previous numerical and experimental studies in the literature.^{48–50} It should be noted here, that the analytical solution for the

meniscus velocity (V_{m-an} in Eq. 13), can capture the initial acceleration observed in the present, and in other studies, only due to the initial zero velocity value at time $t=0$: for very small, but non-zero, values of time, the velocity magnitude will be substantially elevated to infinite values, as it is inversely proportional to this variable. For plotting purposes of V_{m-an} in the present case the choice of the initial time point after the zero value ($t=0.08$ s) was made to avoid infinite velocities.

The dominance of the surface tension forces in the initial part of the flow is indicated by the capillary number, which was estimated using the high shear viscosity ($\mu \approx 0.006$ Pa s, Figure 7), a mean value of 14 mm s^{-1} (from the meniscus velocity \bar{V}_m in the initial stages of the flow - Figure 8b) and the surface tension σ for WB (0.020 Nm^{-1}): $Ca = \frac{\mu \bar{V}_{m-mean}}{\sigma} = 4.2 \cdot 10^{-3}$. There are other forces which potentially contribute to this initial transient behaviour. The fluid drop volume placed at the entrance of the channel was considerably larger than the channel volume ($50 \text{ }\mu\text{L}$ to $0.3 \text{ }\mu\text{L}$, respectively) and the diameter of the droplet was approximately 6 mm . Therefore, it is reasonable to expect that an extra, albeit small, surface tension-dependent pressure contribution exists, due to the formed drop at the entrance.^{4,51} Furthermore, a height difference ($\sim 3 \text{ mm}$) between the centres of the channel and the blood drop imply a slight hydrostatic pressure contribution (typically negligible). The aforementioned forces although negligible may contribute positively to the flow and may explain the meniscus acceleration during the initial stages of the flow in this particular case and in general.

When deriving the analytical solution for the meniscus velocity V_{m-an} (Eq. 13) it was stated that the mean velocity in the core of the flow should be equal to the meniscus velocity (\bar{V}_m). The mean velocity in the core of the channel flow (\bar{V}_{ch}) was calculated from the μPIV -measured velocity profiles (the velocity profiles, V_{ch} , are presented in the next section). \bar{V}_{ch} is a good approximation of the meniscus velocity, and was calculated by integrating the velocity profile along the x direction, divided by the width of the channel:

$$\bar{V}_{ch} = \frac{1}{W} \int_{-W/2}^{W/2} V_{ch} \, dx.$$

\bar{V}_{ch} was compared to the analytical solution V_{m-an} for the meniscus velocity in the graph of Figure 8b (red triangles). Quantitative differences exist between the experimental observations and analytical solution, however, a very good agreement is observed for times beyond 1 s .

3.2 Velocity profiles in the core of the flow

Velocity profiles were extracted from the measured velocity vectors, within the region of interest shown in Figure 3d. The velocity vectors were averaged spatially in the z-direction and temporally for the duration of the flow (ensemble averaging) to yield the velocity profile. The resulting velocity profiles (V_{ch}) are shown in Figure 9 for all the fluids tested. All profiles have been normalised with their maximum values (\bar{V}_{ch}^*) and the Newtonian analytical solution V_{z-c} (Eq. 14) is also included for comparison. In general the velocity profiles in the core of the flow followed the expected paraboloid behaviour for all the fluids investigated, due to the no-slip conditions at the boundaries, in agreement with other capillary- and pressure-driven microfluidic studies.^{4,52,53} Zero velocity at the side-walls has been assumed, and the velocity profiles in Figure 9 have been extended to this value.

In Figure 9a the ensemble average profiles have been calculated for the whole duration of the test (~1.6 s) and as the figure illustrates no significant differences exist between the cases. A difference, however, is apparent between the experimental and the analytical curves. Panels b, c, and d in Figure 9 show the ensemble average of the velocity profiles for different time periods in the flow. As Figure 8b illustrates the velocity of the fluids decreases with time and therefore it is of interest to assess any time influence on the velocity profile, as it is well known that RBC aggregation is a time and shear-dependent phenomenon.⁵⁴ The velocity profile calculated by the analytical solution is used as the reference condition. Inspecting the WB case (panel 9b) it is observed that the profile for the late time period (Δt_2) is blunter, when compared to the one calculated at an earlier time period Δt_1 . The difference is significant for part of the channel width, and can be explained by the influence of the red blood cell aggregation phenomenon which is more intense at the lower shearing conditions. For the non-Newtonian fluids, the shearing forces are proportional to the velocity gradient in the flow in a non-linear manner (the power law model used in this study is an example) resulting in higher flow resistance at regions of lower shear.

Smaller differences between the profiles at the different time periods (Δt_1 and Δt_2) are observed in the other two fluids (NF and NAB, Figures 9c and 9d respectively). The velocity profiles for the NF case approaches the analytical one as expected. A comparison between the WB and NAB profiles, shows that the velocity profile of WB is closer to the blunter, analytical profile. This is in agreement with the behaviour

of aggregating blood observed in previous studies⁹: in a pressure driven flow of an aggregating blood sample in a rectangular microchannel, the velocity profile is blunter than that of the non-aggregating blood, in both simulated (CFD) and experimental flows.

Figure 9

3.3 Structural characteristics

In order to estimate the extend of RBC aggregation in the measured WB flows the intensity coefficient of variation, CV_I , was calculated as the ratio between the Intensity standard deviation (SD_I) and the mean intensity (\bar{I}) in the ROI of the image: $CV_I = \frac{SD_I}{\bar{I}}$. RBC aggregation causes changes in the image intensity characteristics, which can be captured by the statistical variance and illustrated with CV_I . Figure 10 shows a clear difference between the aggregating case (WB) and the other two cases (NF and NAB). The CV_I for the NAB and the NF cases fluctuate around 0.23, whereas the CV of the WB case increases from 0.26 to 0.29 almost monotonically. This increase is expected as it is well known that RBC aggregation is a shear and time-dependent function.⁵⁵

Figure 10

In previous studies^{9,10} aggregating blood has also shown an increase in velocity bluntness compared to non-aggregating samples. Large aggregates concentrate at the centre of the flow resulting in an increase in viscosity therein compared to the near wall regions.¹³ The increased viscosity at the centre of the channel causes a decrease in the velocity therein. Hence, the decrease in the velocity around the centre results in a blunter velocity profile. As erythrocyte aggregation is significantly influenced by inflammation sensitive properties it may be considered as a clinically relevant parameter in this study. However, since blood from a healthy donor was used in the present study and the intensity of aggregation therein is at physiological levels, no robust conclusions can be made on the clinical significance of the phenomenon.

3.4 Shearing conditions

RBC aggregation is a shear and time dependent phenomenon and therefore it is of interest to estimate the shearing conditions in the channel. The shear rate magnitude in the microchannel can be evaluated from the individual shear strain components.⁵⁶

$$|\dot{\gamma}| = \left[2 \left(\frac{\partial u}{\partial x} \right)^2 + 2 \left(\frac{\partial w}{\partial z} \right)^2 + 2 \left(\frac{\partial v}{\partial y} \right)^2 + \left(\frac{\partial w}{\partial x} + \frac{\partial u}{\partial z} \right)^2 + \left(\frac{\partial v}{\partial z} + \frac{\partial w}{\partial y} \right)^2 + \left(\frac{\partial u}{\partial y} + \frac{\partial v}{\partial x} \right)^2 \right]^{\frac{1}{2}}. \quad (15)$$

If it is assumed that the u and v components are negligible (i.e. one-dimensional flow) and flow is fully developed ($\frac{\partial}{\partial z} = 0$) then the equation for $|\dot{\gamma}|$ becomes:

$$|\dot{\gamma}| = \left[\left(\frac{\partial w}{\partial x} \right)^2 + \left(\frac{\partial w}{\partial y} \right)^2 \right]^{\frac{1}{2}} \quad (16)$$

The first term (the in-plane shear rate component) can be calculated from the experimental velocity profile as follows; $\dot{\gamma}_{i-p} = \frac{\partial w}{\partial x} = \frac{dV_{ch}}{dx}$. The out-of-plane shear rate component ($\dot{\gamma}_{o-p} = \frac{\partial w}{\partial y}$) was estimated as $\frac{V_{max}}{2h}$ where V_{max} is the maximum velocity in the experimental velocity profile (V_{ch}), and $2h$ the channel height ($100\mu\text{m}$). $|\dot{\gamma}|$ is shown in Figure 11 as fitted curves on the experimental data. Moderate to strong shear conditions occur closer to the walls reaching magnitudes of more than 90 s^{-1} . Studies on normal RBC aggregation kinetics in shear flow⁵⁷ have shown that for healthy human RBCs the disaggregation process starts from $\dot{\gamma} = 2.5 \text{ s}^{-1}$, whereas other studies⁵⁸ have shown that a critical disaggregation shear rate lies between $\dot{\gamma} \sim 70 \text{ s}^{-1}$ and 150 s^{-1} . Furthermore, since the μPIV technique underestimates the calculated velocities, the actual shearing conditions are expected to be further elevated.

Figure 11

Therefore, the shear conditions developed in the microchannel, especially close to the walls and during the initial time periods, are sufficiently strong to keep RBC aggregation at low levels. The value of CV_1 (Figure 10) of the aggregating sample increased approximately 15% compared to the PBS value at the initial stages of the flow, reaching a difference of approximately 27% at the final stages.

4 Limitations

In the bright field μPIV technique there is a certain degree of error due to the large depth of correlation of the microscope objective. This finite depth of correlation leads to an underestimation of the velocity magnitude, the extent of which was assessed in the present study and agrees with previous reports (discussed earlier in section 2.6). Nevertheless, as it can be observed in Figure 5, the velocity underestimation is seen to be consistent across the flow field and therefore the shape of the velocity profile should be qualitatively preserved.

The side walls of the channel are constructed by a double-sided adhesive tape, which introduces an apparent roughness on the side wall-flow interface. As a result, an uncertainty in the exact location of the wall exist and the local flow may be influenced in this region. For this reason, the PIV analysis was performed on the flow field indicated by the ROI in Figure 3d, and the velocity profiles were extended to an assumed zero value (no slip) at the walls of the channel, i.e. at $x^* = 0.5$.

The sample deposition at the entrance of the channel is conducted with great care by the trained operator using a micropipette. The sample volume is consistently controlled using the micropipette, however uncertainties due to sample handling might be possible. In the present work, cases showing abnormal behaviour (mainly abnormal meniscus velocity at the entrance) have been excluded from the analysis.

Viscosity values at the lowest shear rate (12.5 s^{-1}) were close to the lower sensitivity limit of the viscometer (accepted at the 5% of the transducer torque range). Nevertheless, the viscosity of the Newtonian fluid measured in this low-end of the torque sensitivity, shows no significant deviation from the rest of values indicating valid readings of viscosity for WB and NAB fluids.

5 Conclusions

In the present study, the influence of red blood cell aggregation on surface tension driven flows in a rectangular micro channel was examined. Newtonian fluid, non-aggregating and aggregating blood samples were tested and the flow characteristics in the micro channel were analysed and compared, through micro-PIV based techniques and analytical solutions. RBC aggregation was found to have an influence on the flow characteristics as manifested by the velocity profile bluntness. Moderate to strong shear rates were observed in the initial stages of the flow determining the extent of aggregation present in the channel. The present results illustrate that red blood cell aggregation should be considered as an influencing factor in passive microchannel blood flows akin to those used in many point of care diagnostics.

Acknowledgments

The study has been supported by funding from the internal Start-Up Grants of the Cyprus University of Technology, by a grant from the Cyprus Research and Innovation Foundation (ref.: EXCELLENCE

This is the author's peer reviewed, accepted manuscript. However, the online version of record will be different from this version once it has been copyedited and typeset.
PLEASE CITE THIS ARTICLE AS DOI:10.1063/1.50008939

/0918/0215), and by funding from the Youth Board of Cyprus (Dimitris Pasiias scholarship).

Author Contributions

All authors contributed to this work

Data availability

Data, subject to ethical restrictions, available on request from the authors.

References

- ¹ E.K. Sackmann, A.L. Fulton, and D.J. Beebe, *Nature* **507**, 181 (2014).
- ² B. Weigl, G. Domingo, P. Labarre, and J. Gerlach, *Lab Chip* **8**, 1999 (2008).
- ³ J.H. Tsui, W. Lee, S.H. Pun, J. Kim, and D.H. Kim, *Adv. Drug Deliv. Rev.* **65**, 1575 (2013).
- ⁴ E. Berthier and D.J. Beebe, *Lab Chip* **7**, 1475 (2007).
- ⁵ J.G. Santiago, S.T. Wereley, C.D. Meinhart, D.J. Beebe, and R.J. Adrian, *Exp. Fluids* (1998).
- ⁶ A.G. Koutsiaris, D.S. Mathioulakis, and S. Tsangaris, *Meas. Sci. Technol.* (1999).
- ⁷ R. Lima, S. Wada, K.I. Tsubota, and T. Yamaguchi, *Meas. Sci. Technol.* **17**, 797 (2006).
- ⁸ R. Lima, T. Ishikawa, Y. Imai, M. Takeda, S. Wada, and T. Yamaguchi, *J. Biomech.* **41**, 2188 (2008).
- ⁹ J.M.M. Sherwood, J. Dusting, E. Kaliviotis, and S. Balabani, *Biomicrofluidics* **6**, (2012).
- ¹⁰ J.M. Sherwood, E. Kaliviotis, J. Dusting, and S. Balabani, *Biomech. Model. Mechanobiol.* **13**, 259 (2014).
- ¹¹ J.M.J.M. Sherwood, D. Holmes, E. Kaliviotis, and S. Balabani, *PLoS One* **9**, (2014).
- ¹² E. Kaliviotis, D. Pasiadis, J.M. Sherwood, and S. Balabani, *Med. Eng. Phys.* (2016).
- ¹³ E. Kaliviotis, J.M. Sherwood, and S. Balabani, *Sci. Rep.* **7**, (2017).
- ¹⁴ E. Kaliviotis, J.M. Sherwood, and S. Balabani, *Phys. Fluids* **30**, (2018).
- ¹⁵ G. Tomaiuolo, L. Lanotte, G. Ghigliotti, C. Misbah, and S. Guido, *Phys. Fluids* **24**, (2012).
- ¹⁶ R. D'Apolito, F. Taraballi, S. Minardi, X. Liu, S. Caserta, A. Cevenini, E. Tasciotti, G. Tomaiuolo, and S. Guido, *Med. Eng. Phys.* **38**, 17 (2016).
- ¹⁷ R. Mehri, J. Laplante, C. Mavriplis, and M. Fenech, *J. Med. Biol. Eng.* **34**, 469 (2014).
- ¹⁸ R. Mehri, C. Mavriplis, and M. Fenech, *PLoS One* (2018).
- ¹⁹ W.H. Reinhart, N.Z. Piety, and S.S. Shevkoplyas, *Microcirculation* DOI: 10.1111/micc.12317 (2016).
- ²⁰ J. Berthier, K.A. Brakke, E.P. Furlani, I.H. Karampelas, V. Poher, D. Gosselin, M. Cubizolles, and P.

- Pouteau, *Sensors Actuators, B Chem.* **206**, 258 (2015).
- ²¹ S. Cito, Y.-C. Ahn, J. Pallares, R.M. Duarte, Z. Chen, M. Madou, and I. Katakis, *Microfluid. Nanofluidics* **13**, 227 (2012).
- ²² P. Krause, *J. Chem. Educ.* (2000).
- ²³ C.K. Chung, Y.S. Chen, and T.R. Shih, *Microfluid. Nanofluidics* (2009).
- ²⁴ B. Ruben, M. Elisa, L. Leandro, M. Victor, G. Gloria, S. Marina, S. Mian K, R. Pandiyan, and L. Nadhira, *Micro Nano Lett.* (2017).
- ²⁵ A.U. Alam, M.M.R. Howlader, and M.J. Deen, *J. Micromechanics Microengineering* (2014).
- ²⁶ S. Luo and C.P. Wong, *IEEE Trans. Components Packag. Technol.* (2001).
- ²⁷ M. Sneha Maria, P.E. Rakesh, T.S. Chandra, and A.K. Sen, *Biomicrofluidics* **10**, 1 (2016).
- ²⁸ H.M. Kim, S.B. Seo, D.Y. Kim, K. Bae, and S.Y. Sohn, *Trans. Electr. Electron. Mater.* (2013).
- ²⁹ Y.F. Chen, F.G. Tseng, S.Y. ChangChien, M.H. Chen, R.J. Yu, and C.C. Chieng, *Microfluid. Nanofluidics* **5**, 193 (2008).
- ³⁰ C.F. Kung, C.F. Chiu, C.F. Chen, C.C. Chang, and C.C. Chu, *Microfluid. Nanofluidics* **6**, 693 (2009).
- ³¹ N. Ichikawa, K. Hosokawa, and R. Maeda, *J. Colloid Interface Sci.* **280**, 155 (2004).
- ³² W. Huang, R.S. Bhullar, and Yuan Cheng Fung, *J. Biomech. Eng.* (2001).
- ³³ S. Chakraborty, *Lab Chip* **5**, 421 (2005).
- ³⁴ J. Wang, W. Huang, R.S. Bhullar, and P. Tong, *Mech. Chem. Biosyst.* **1**, 161 (2004).
- ³⁵ K. Lee, M. Kinnunen, M.D. Khokhlova, E. V Lyubin, A. V Priezhev, I. Meglinski, and A.A. Fedyanin, *J. Biomed. Opt.* **21**, 35001 (2016).
- ³⁶ O.K. Baskurt and H.J. Meiselman, *Semin. Thromb. Hemost.* **29**, 435 (2003).
- ³⁷ W. Kowalczyk, B.E. Zima, and A. Delgado, *Exp. Fluids* **43**, 147 (2007).
- ³⁸ D. Juncker, H. Schmid, U. Drechsler, H. Wolf, M. Wolf, B. Michel, N. De Rooij, and E. Delamarche,

This is the author's peer reviewed, accepted manuscript. However, the online version of record will be different from this version once it has been copyedited and typeset.
PLEASE CITE THIS ARTICLE AS DOI:10.1063/1.50008939

- Anal. Chem. **74**, 6139 (2002).
- ³⁹ S. Cito, J. Pallares, A. Fabregat, and I. Katakis, *Int. Commun. Heat Mass Transf.* (2012).
- ⁴⁰ Y. Yuan and T.R. Lee, in *Surf. Sci. Tech.* (2013), pp. 3–5.
- ⁴¹ C.J. Bourdon, M.G. Olsen, and A.D. Gorby, *J. Fluids Eng.* **128**, 883 (2006).
- ⁴² C. Poelma, A. Kloosterman, B.P. Hierck, and J. Westerweel, *PLoS One* **7**, (2012).
- ⁴³ S. Zhang, N. Cagney, S. Balabani, C.P. Naveira-Cotta, and M.K. Tiwari, *Phys. Fluids* (2019).
- ⁴⁴ S. Zhang, C. Neil, T. Lacassagne, C.P. Balabani, Stavroula Naveira-Cotta, and M.K. Tiwaria, *Chem. Eng. J.* **Accepted**, (2020).
- ⁴⁵ C.T. Crowe, J.D. Schwarzkopf, M. Sommerfeld, and Y. Tsuji, *Multiphase Flows with Droplets and Particles* (2011).
- ⁴⁶ M.A. Elblbesy and A.T. Hereba, *Appl. Phys. Res.* (2016).
- ⁴⁷ H. Bruus, *Theoretical Microfluidics* (Oxford University Press, USA, 2008).
- ⁴⁸ G. Cavaccini, V. Pianese, A. Jannelli, S. Iacono, and R. Fazio, *J. Comput. Methods Sci. Eng.* **9**, 3 (2009).
- ⁴⁹ J. Szekely, A.W. Neumann, and Y.K. Chuang, *J. Colloid Interface Sci.* (1971).
- ⁵⁰ N. Srivastava and M.A. Burns, *Anal. Chem.* **78**, 1690 (2006).
- ⁵¹ S. Zaitsev, *Adv. Colloid Interface Sci.* (2016).
- ⁵² A.R. Pries, D. Neuhaus, and P. Gaehtgens, *Am. J. Physiol. - Hear. Circ. Physiol.* **263**, H1770 (1992).
- ⁵³ J.M.J.M. Sherwood, D. Holmes, E. Kaliviotis, and S. Balabani, *PLoS One* **9**, (2014).
- ⁵⁴ E. Kaliviotis and M. Yianneskis, *Clin. Hemorheol. Microcirc.* **39**, (2008).
- ⁵⁵ E. Kaliviotis and M. Yianneskis, *Biorheology* **46**, 487 (2009).
- ⁵⁶ E. Kaliviotis, J. Dusting, and S. Balabani, *Med. Eng. Phys.* **33**, (2011).
- ⁵⁷ N.N. Firsov, A. V. Priezhev, and O.M. Ryaboshapka, in *Proc. SPIE - Int. Soc. Opt. Eng.* (1993).

This is the author's peer reviewed, accepted manuscript. However, the online version of record will be different from this version once it has been copyedited and typeset.

PLEASE CITE THIS ARTICLE AS DOI:10.1063/1.50008939

⁵⁸ P. Snabre, M. Bitbol, and P. Mills, Biophys. J. **51**, 795 (1987).

Figures

Figure 1

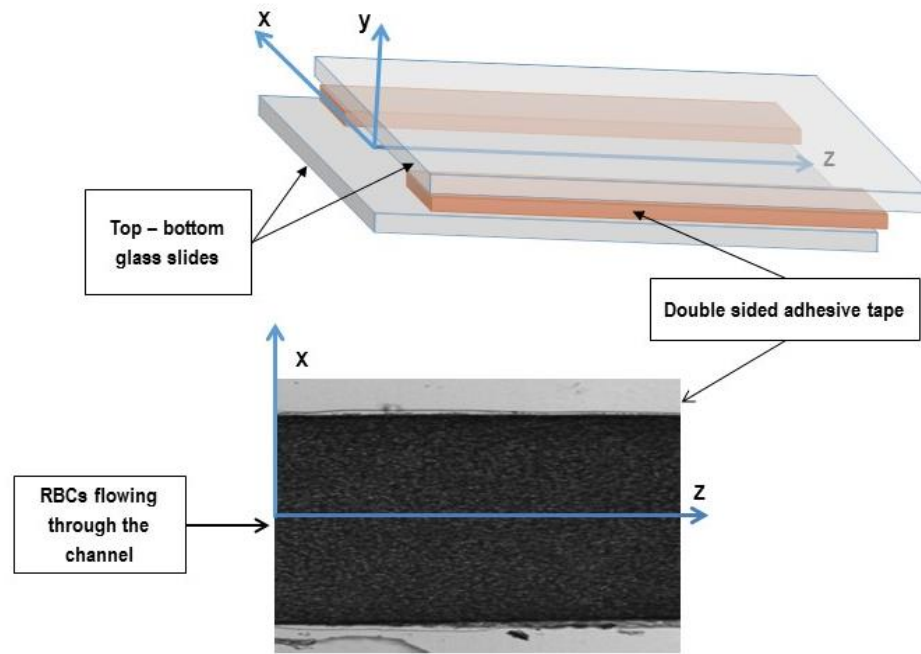


FIG 1. Top: Schematic of the microchannel geometry (not in scale) and the coordinate system used.

Bottom: Sample image of the RBC flow in the microchannel.

This is the author's peer reviewed, accepted manuscript. However, the online version of record will be different from this version once it has been copyedited and typeset.
PLEASE CITE THIS ARTICLE AS DOI:10.1063/1.50008939

Figure 2

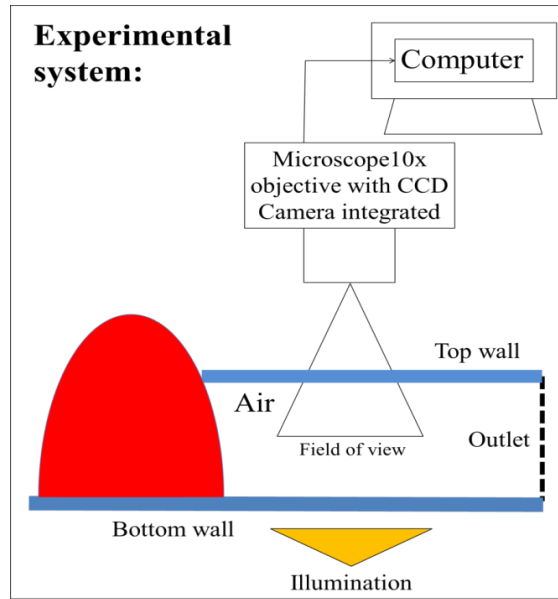


FIG. 2. Annotated schematic of the capillary driven micro channel flow, and the μ PIV measurement set up: the gap ($2h$) between the top and bottom walls of the channel was $100\ \mu\text{m}$, respectively (diagram not to scale).

This is the author's peer reviewed, accepted manuscript. However, the online version of record will be different from this version once it has been copyedited and typeset.
 PLEASE CITE THIS ARTICLE AS DOI:10.1063/1.50008939

Figure 3

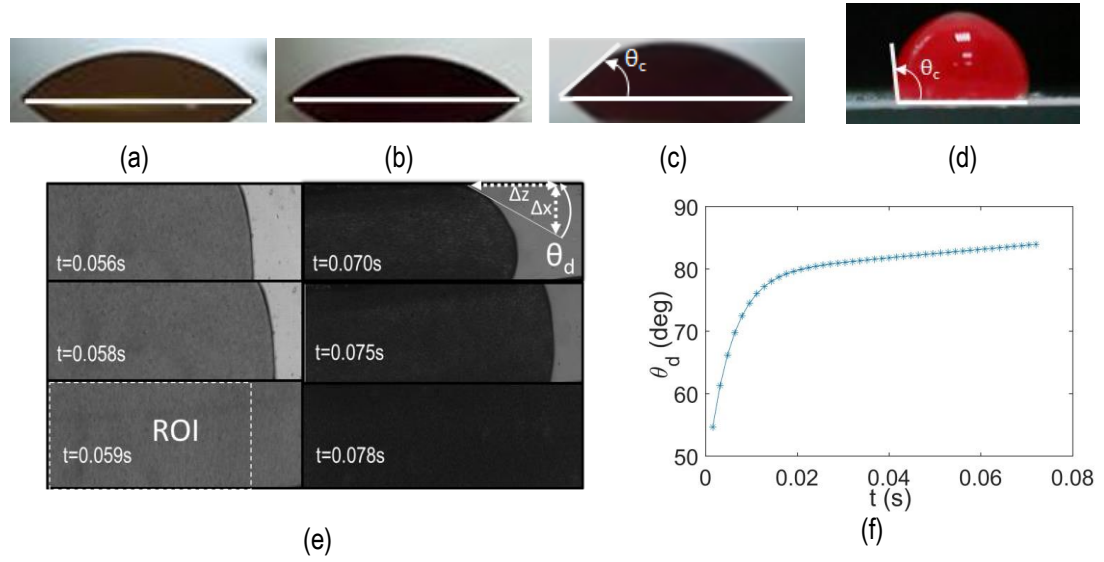


FIG. 3. Top panels: Images of drops from the Newtonian fluid (a), the non-aggregating blood (b), and whole blood (c) on the glass surface. θ_c is the measured static contact angle. In panel (d): Representative image of whole blood drop on the adhesive tape. Panel (e): Images of whole blood (right) and Newtonian fluid flow (left), showing the meniscus shape and the region of interest in which the velocity profiles were derived; the dynamic contact angle is shown on the top-right channel. Panel (f): Dynamic contact angle θ_d (in degrees) as a function of time.

This is the author's peer reviewed, accepted manuscript. However, the online version of record will be different from this version once it has been copyedited and typeset.
 PLEASE CITE THIS ARTICLE AS DOI:10.1063/1.50008939

Figure 4

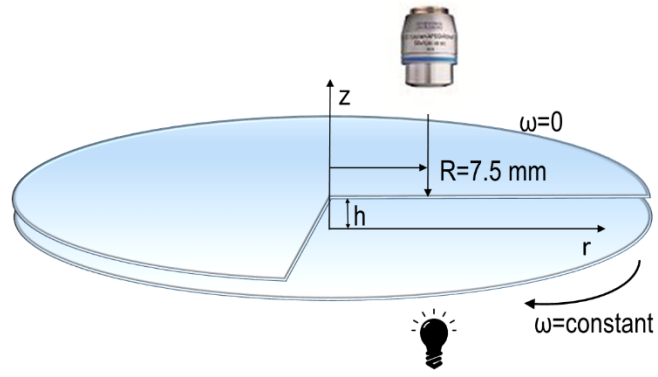


FIG. 4. Schematic of plate-plate system.

This is the author's peer reviewed, accepted manuscript. However, the online version of record will be different from this version once it has been copyedited and typeset.

PLEASE CITE THIS ARTICLE AS DOI:10.1063/1.50008939

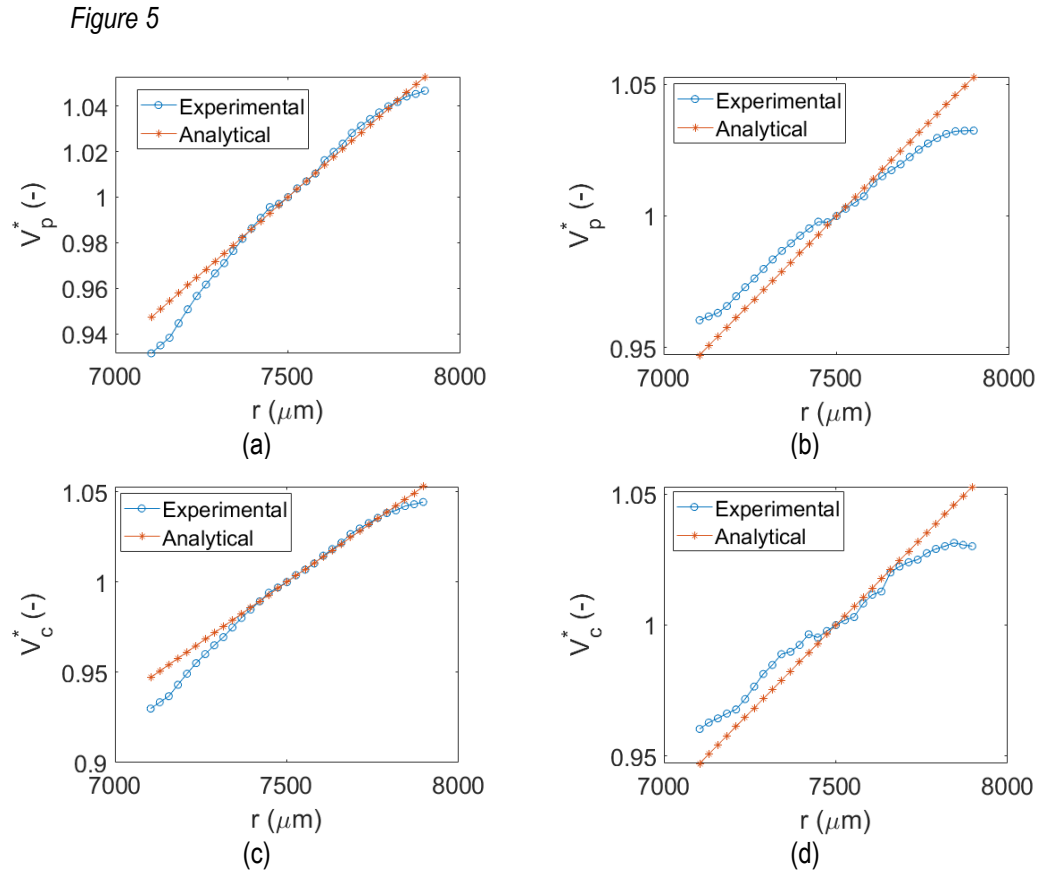


FIG. 5. Top panels: Experimental vs analytical velocity V_p^* (normalised with velocity values at the centre of the flow) for whole blood rotating on the bottom plate at $\omega=0.13$ rad/s (a), and $\omega=0.8$ rad/s (b) (absolute velocities differ by 10.30% and 30.52% respectively). Bottom panels: Experimental vs analytical velocity V_c^* (normalised with velocity values at the centre of the flow) derived from the Couette flow with shear rates 10 s^{-1} ($\omega=0.13$ rad/s) (c) and 60 s^{-1} ($\omega=0.8$ rad/s) (d) (absolute velocities differ by 21.06% and 28.46 % respectively).

This is the author's peer reviewed, accepted manuscript. However, the online version of record will be different from this version once it has been copyedited and typeset.

PLEASE CITE THIS ARTICLE AS DOI:10.1063/1.50008939

Figure 6

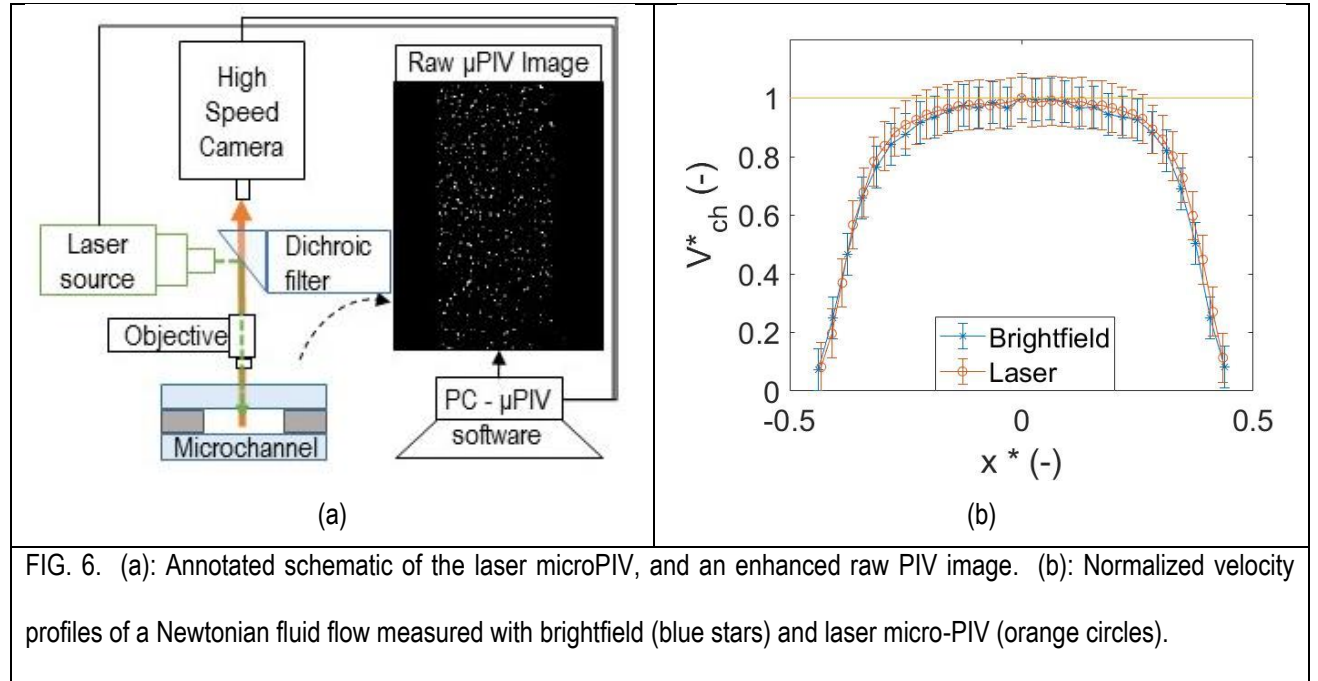


FIG. 6. (a): Annotated schematic of the laser microPIV, and an enhanced raw PIV image. (b): Normalized velocity profiles of a Newtonian fluid flow measured with brightfield (blue stars) and laser micro-PIV (orange circles).

This is the author's peer reviewed, accepted manuscript. However, the online version of record will be different from this version once it has been copyedited and typeset.
PLEASE CITE THIS ARTICLE AS DOI:10.1063/1.50008939

Figure 7

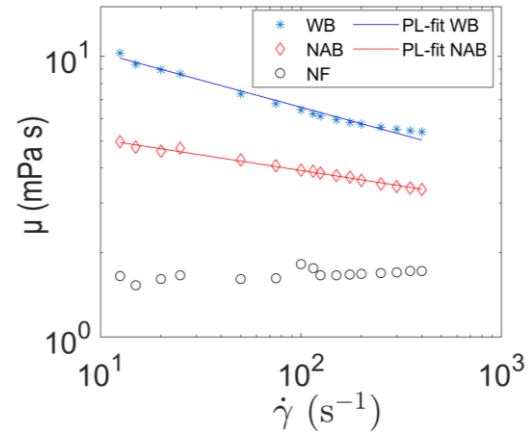


FIG. 7. Viscosity of WB (stars), NAB (diamonds) and NF (circles) at shear rates from 12.5 s^{-1} to 400 s^{-1} .

This is the author's peer reviewed, accepted manuscript. However, the online version of record will be different from this version once it has been copyedited and typeset.

PLEASE CITE THIS ARTICLE AS DOI:10.1063/1.50008939

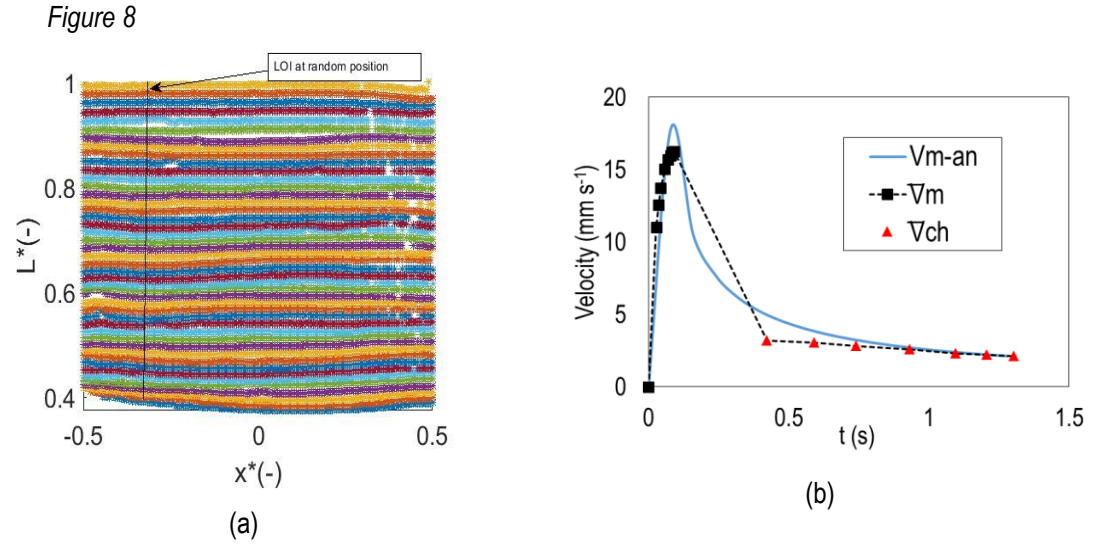


FIG. 8. (a): Normalised meniscus distance ($L^*=L/1.7$ mm) from the entrance of the channel, across the width of the channel. b) Mean velocity values, \bar{V}_m (black rectangles) and \bar{V}_{ch} (red triangles) as a function of time. The solid blue line represents the analytical solution V_{m-an} (Eq. 13), with first non-zero value at 0.08 s. The black dashed line connects the experimental data (not a fitted line). Data produced from a representative WB sample.

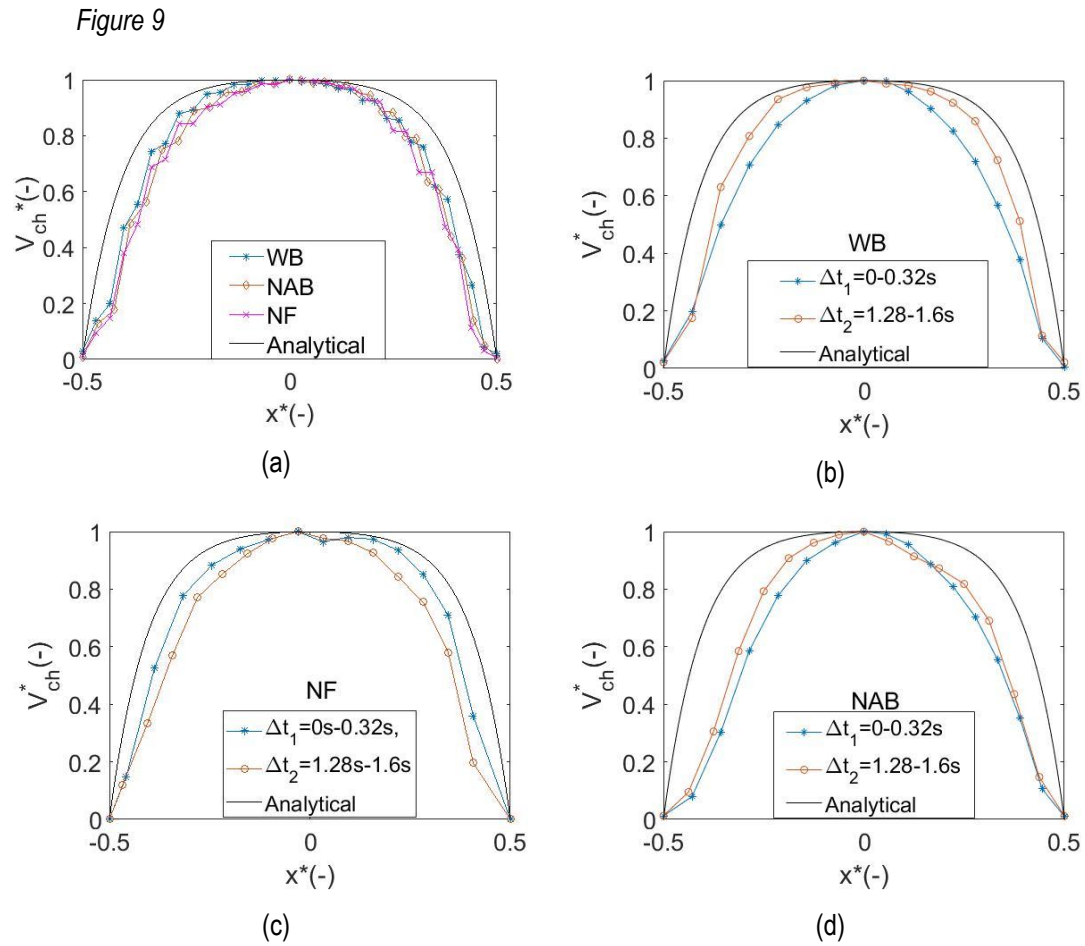


FIG. 9. Velocity profiles for WB, NAB, and NF samples at a microchannel aspect ratio of 3.5. All profiles have been normalized with the maximum velocity value in the profiles. (a): Ensemble average of the profiles of all samples for the whole duration of the flow. (b, c and d): Results for WB, NAB, and NF samples respectively for different time periods in the flow (Δt_1 and Δt_2). The analytical solution is also shown in all graphs for comparison. A zero velocity at the side walls has been assumed in all profiles.

This is the author's peer reviewed, accepted manuscript. However, the online version of record will be different from this version once it has been copyedited and typeset.

PLEASE CITE THIS ARTICLE AS DOI:10.1063/1.50008939

Figure 10

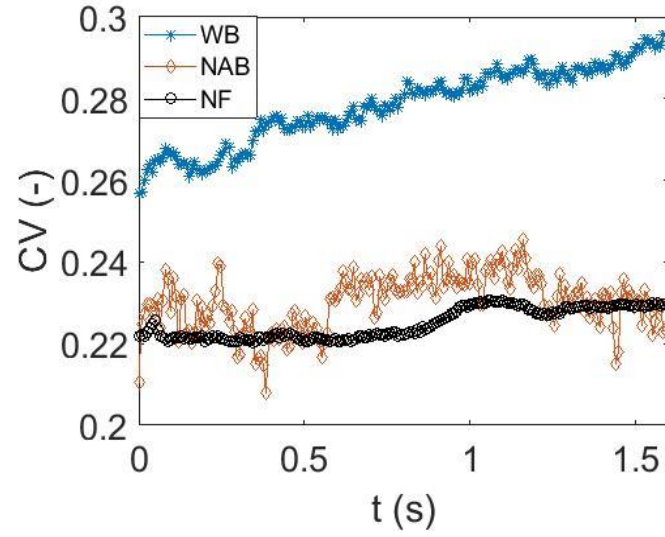


FIG. 10. Coefficient of variation of image intensity as a function of time for flow of WB, NAB and NF samples respectively.

This is the author's peer reviewed, accepted manuscript. However, the online version of record will be different from this version once it has been copyedited and typeset.
PLEASE CITE THIS ARTICLE AS DOI:10.1063/1.50008939

Figure 11

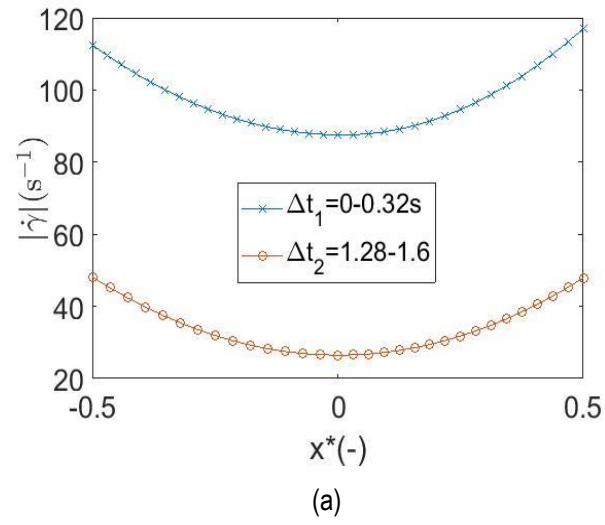
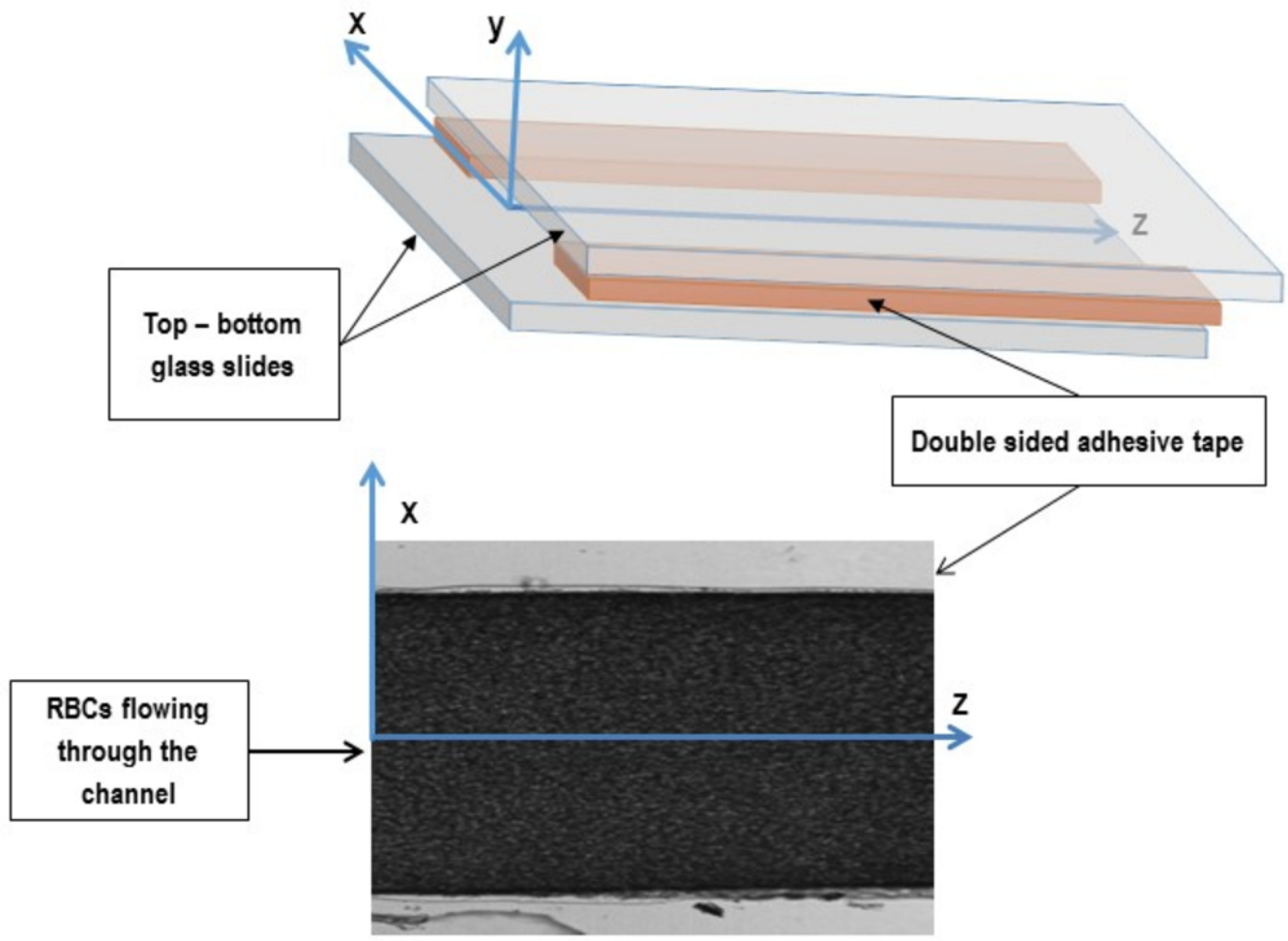
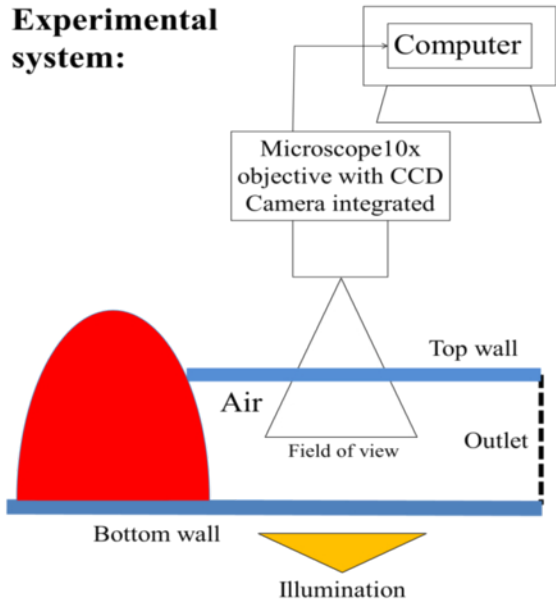
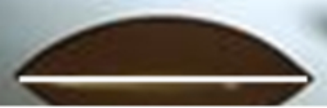


FIG. 11. Profiles of $|\dot{\gamma}|$ across the width of the channel at two different time periods Δt_1 and Δt_2 (lines fitted on experimental data).

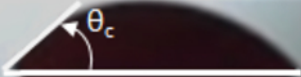


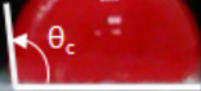
Experimental system:











t=0.056s

t=0.070s

Δz

Δx

θ_d

t=0.058s

t=0.075s

t=0.059s

ROI

t=0.078s

